Magnetic properties of $U_{14}Au_{51}$: an exemplary study by muon spin-rotation (μSR) spectroscopy

1998 J. Phys.: Condens. Matter 10 8059

(http://iopscience.iop.org/0953-8984/10/36/015)

J. Phys.: Condens. Matter **10** (1998) 8059–8082. Printed in the UK PII: S0953-8984(98)94329-6

Magnetic properties of $U_{14}Au_{51}$: an exemplary study by muon spin-rotation (μSR) spectroscopy

A Schenck†, M Pinkpank†, F N Gygax†, K-U Neumann‡, K R A Ziebeck‡ and A Amato§

† Institute for Particle Physics of ETHZ, CH-5232 Villigen PSI, Switzerland

‡ Department of Physics, Loughborough University, Loughborough, Leicestershire LE11 3TU, UK

§ Paul Scherrer Institute (PSI), CH-5232 Villigen PSI, Switzerland

Received 13 May 1998, in final form 1 July 1998

Abstract. The results of a muon spin-rotation (μSR) study of single-crystalline $U_{14}Au_{51}$ in the paramagnetically and antiferromagnetically (AF) ordered phases are reported. Transverse-field measurements for the paramagnetic phase reveal four components in the μSR signal, distinguished by their different Knight shifts, which can be associated with two crystallographically different sites: a magnetically unique site in the $z = \frac{1}{2}$ plane near the position (0 0 $\frac{1}{2}$), i.e. between two U3 ions, and a site with a threefold symmetry near the centre of a triangle formed by three U1 ions, located in the $z = \frac{1}{2}$ plane. It appears that the U3 ions are nearly, but not entirely, non-magnetic also in the paramagnetic phase. The temperature dependence of the different μ^+ Knight shifts follows a Curie–Weiss law but it involves significantly different Curie–Weiss temperatures as compared with the bulk susceptibility, which even show an anisotropy in the hexagonal a–b plane. This does not seem to be a μ^+-induced feature but is rather a consequence of selectively monitoring just the magnetic response of the U1 ions. In the AF state below $T_N = 22$ K, measurements reveal two different spontaneous internal magnetic fields which can be traced back to the two different sites, thus confirming the non-collinear complex AF structure recently found by neutron scattering.

1. Introduction

The hexagonal compound $U_{14}Au_{51}$ (space group $P6/m$) is classified as a moderately heavy-electron compound ($\gamma \simeq 300$ mJ K^{-2}/mol U) and has been shown by susceptibility, specific heat and resistivity measurements to undergo a magnetic phase transition at 22 K [1]. In contrast to other heavy-electron U compounds, $U_{14}Au_{51}$ is special in that there are three crystallographically distinct U sites in this crystal, namely the sites 6k, 6j and 2e, labelled as U1, U2 and U3 respectively. In fact, a first neutron powder diffraction investigation of the antiferromagnetic (AF) magnetic structure of $U_{14}Au_{51}$ demonstrated different ordered magnetic moments associated with the different sites [2]. In particular, no moment was associated with the U3 ions at the 2e sites. This was explained as arising due to the rather small distance between two U3 ions along the c-axis which allows for a direct overlap of the f-electron wave functions and the formation of a non-magnetic spin-singlet state. Recently a new detailed neutron scattering investigation [3], combining neutron polarimetry with integrated intensity measurements on a single-crystal sample, implied a much more complex AF magnetic structure than the one proposed in reference [2]. According to these new results, the AF magnetic structure is non-collinear and the U moments are confined

0953-8984/98/368059+24$19.50

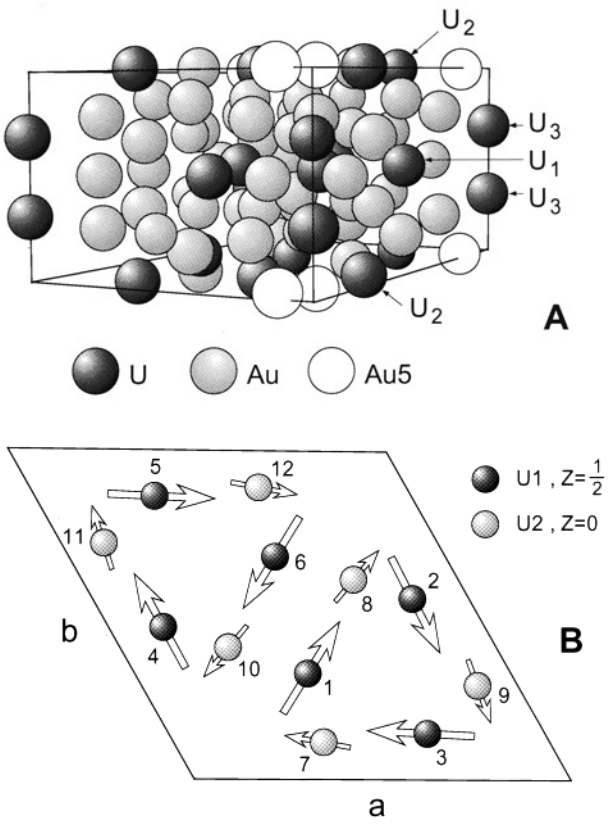

Figure 1. (A) A schematic representation of the structure of $U_{14}Au_{51}$. (B) The arrangement of the U1 atoms in the $z = 1/2$ plane and of the U2 atoms in the $z = 0$ plane. Also shown by the arrows is the non-collinear antiferromagnetic structure below $T_N = 22$ K. The length of the arrows is proportional to the ordered moment value (from reference [3]).

to the *a*–*b* plane (in reference [2] it was proposed that the moments are aligned along the *c*-axis with zero propagation vector). In agreement with reference [2], no ordered moments are associated with the U3 ions. The moments at the two sets (U1, U2) of sixfold sites are arranged hexagonally (e.g. around the (001) axis) with rotations of 60° between them and the two sets are rotated with respect to one another by 50° (see figure 1). At the U1 sites the ordered moment for $T \rightarrow 0$ K is determined as 2.28(7) μ_B and at the U2 sites as 1.48(8) μ_B.

Reference [3] also provides detailed results on the magnetic susceptibility in the paramagnetic state, summarized in table 1. As can be seen, the paramagnetic Curie–Weiss temperatures are anisotropic with respect to the *c*-axis. The susceptibility measurements do not allow us to determine the individual magnetic response of the different types of U ion.

The rich and by now well understood magnetic structure of $U_{14}Au_{51}$ renders it a challenging testing ground for a local probe technique, such as muon spin rotation (μSR). First, can μSR be used to confirm such a complex magnetic structure and, secondly, is it sensitive enough to, e.g., distinguish between the structures proposed in references [2] and [3] thereby removing possible ambiguities which are sometimes encountered in neutron scattering? Also, is it possible to learn something about the magnetic response of the U

Table 1. Curie–Weiss parameters. (θ = Curie–Weiss temperature; $p_{eff} = J(J+1)g_J$.)

	Polycrystalline	$a(b)$-axis	b^*-axis	c-axis
p_{eff}	3.32	3.19(5)	3.19	3.12(5)
θ (K)	-100	$-71(1)$	-71	$-111(1)$
Reference	[1]	[3]		[3]
θ' (K), site I		$-57(3)$†	$+13(2)$†	-164^{+37}_{-53}
θ' (K), site II		$+11.4(2.4)$†	11.4†	$+26^{+12}_{-19}$†

† These are values for the principal axes of the local susceptibility tensor.

ions at the different sites in the paramagnetic state? And finally, can one study muon-induced modifications of magnetic properties which, of course, are restricted to the nearest μ^+-neighbours?

As will be discussed below, all three aspects are amenable to investigation by the μSR technique [4], provided that the μ^+-site(s) are known. An important part of the present work is therefore concerned with the determination of the μ^+-sites.

In the following we will first present information on some experimental details (section 2), then present and discuss the results obtained for the paramagnetic state, leading to the site determinations (section 3), and those for the AF ordered state, confirming the neutron diffraction results [3] (section 4), and we will conclude with a general discussion in section 5.

Table 2. The samples investigated, with demagnetization factors taken from reference [7].

No	Approximate dimensions $x \times y \times z$ (in mm)	Approximate orientation	N_a (4π)	N_{b^*} (4π)	N_c (4π)
1	$6.7 \times 8 \times 0.85$	a-axis $\parallel \boldsymbol{z}$, c-axis $\parallel \boldsymbol{x}$	0.830		~ 0
2	Diameter ~ 8, length ~ 20	c-axis $\parallel$ long axis	0.45	0.45	0.10
3	$3 \times 3 \times 15$	c-axis $\parallel \boldsymbol{z}$	0.49	0.49	

2. Experimental details

2.1. Samples

All of the single-crystalline samples investigated originated from one rather large single crystal which was grown by the Czochralski method from spectroscopically pure uranium and gold melted together in the appropriate proportions. This material had been used before in the neutron diffraction study of reference [3]. The actual samples used are listed in table 2 together with some estimated relevant demagnetization factors.

2.2. Spectrometers

All of the μSR measurements were performed at the high-intensity proton accelerator of the Paul Scherrer Institute (PSI) in Villigen, Switzerland. For a description of the μSR technique (zero field, transverse field etc), see reference [4]. The transverse-field (TF) measurements on the paramagnetic phase made use of the General Purpose Spectrometer

(GPS) on the surface μ^+-beamline πM3, using samples No 1 and No 3, and the high-precision ETH ('strobo') instrument in the time-differential mode as well as the General Purpose Decay (GPD) spectrometer, both on the conventional decay muon beam line μE1, using sample No 2. Temperatures could be varied between 4 K (10 K) and 300 K using a He-flow cryostat (GPS, 'strobo') or a closed-cycle refrigerator (GPD). The applied fields H_{ext} varied from 4 kOe (GPD) to 6 kOe (GPS, 'strobo'). The 'strobo' instrument and the GPS allow us to rotate the sample around an axis perpendicular to $\boldsymbol{H}_{ext}$. In this way it was possible to rotate $\boldsymbol{H}_{ext}$ in the basal *a–b* plane (samples No 2, No 3) and in the *a–c* plane (sample No 1). In the latter case, the geometry of the sample excluded angles between $\boldsymbol{H}_{ext}$ and the *c*-axis smaller than 30°. In the GPD, $\boldsymbol{H}_{ext}$ was always parallel to the *c*-axis. The external field was measured by an NMR magnetometer or directly by μSR by replacing the $U_{14}Au_{51}$ sample by a non-magnetic Ag target. The stability of the external field was of the order of 10–50 ppm, which is negligible compared to the rather large frequency shifts.

The zero-field (ZF) measurements for the ordered phase used exclusively the GPS and only sample No 1 was investigated.

3. Measurements on the paramagnetic phase

3.1. Some basic considerations

The primary purpose of these measurements was to identify via the temperature and orientational dependence of the μ^+ Knight shift or shifts the μ^+-site(s) involved. The procedure has been described before [5, 6] and we summarize here just a few useful formulae. As usual, the Knight shift K is defined as the fractional shift $\Delta\nu/\nu_0$ of the precession frequency ν relative to the frequency ν_0 in the presence of just the external field $\boldsymbol{H}_{ext}$ ($\nu_0 = (\gamma_\mu/2\pi)H_{ext}$; γ_μ is the gyromagnetic ratio of the μ^+). The shift arises from the conduction electron spin polarization at the μ^+-position resulting in the Fermi contact hyperfine field $\boldsymbol{B}_c$ and from the static moments

$$\boldsymbol{m}_f = \boldsymbol{\chi}_f \boldsymbol{H}_{ext} \tag{1}$$

induced by the external field on the U sites, involving the 5f electrons ($\boldsymbol{\chi}_f$ is the relevant susceptibility tensor), which produce some net dipole field $\boldsymbol{B}_{dip}$ at the μ^+-site. Neglecting higher-order contributions, K is given by

$$K = (\boldsymbol{B}_c + \boldsymbol{B}_{dip}) \cdot \frac{\boldsymbol{H}_{ext}}{H_{ext}^2} \tag{2}$$

and

$$\boldsymbol{B}_{dip} = \sum_i \boldsymbol{B}_{dip,i} = \sum_i \left(\frac{3(\boldsymbol{m}_f \cdot \boldsymbol{r}_i)\boldsymbol{r}_i}{r_i^5} - \frac{\boldsymbol{m}_f}{r_i^3} \right) = \sum_i \mathbf{A}_{dip,i} \boldsymbol{m}_f . \tag{3}$$

That is,

$$\boldsymbol{B}_{dip} = \mathbf{A}_{dip} \boldsymbol{m}_f = \mathbf{A}_{dip} \boldsymbol{\chi}_f \boldsymbol{H}_{ext} . \tag{4}$$

The sum extends over all U neighbours assumed to be magnetically equivalent, inside the Lorentz sphere (see below), and $\boldsymbol{r}_i$ is the distance vector between the μ^+ and the ith U neighbour. $\mathbf{A}_{dip,i}$ and $\mathbf{A}_{dip}$ are dipolar coupling tensors with zero trace. $\mathbf{A}_{dip}$ is a lattice sum over all $\mathbf{A}_{dip,i}$ inside the Lorentz sphere. It is evident that $\mathbf{A}_{dip}$ is completely determined by the crystal structure in question and by the assumed μ^+-position. If magnetically inequivalent but crystallographically equivalent positions are involved, different $\mathbf{A}_{dip}$ will result, but they can be transformed into each other by proper symmetry operations. In

this case the Knight shift will split into different values, i.e. several distinct precession frequencies will show up. An experimental determination of $\mathbf{A}_{dip}$ and its symmetry properties will then allow us to identify the μ^+-position, usually unambiguously.

The conduction electron spin polarization at the μ^+-position is dominated by the induced moments $\boldsymbol{m}_f$ via the RKKY exchange mechanism. Hence we may write

$$\boldsymbol{B}_c = A_0 \boldsymbol{m}_f = A_0 \boldsymbol{\chi}_f \boldsymbol{H}_{ext}. \tag{5}$$

A_0 is the contact coupling constant. A small additional contribution $\boldsymbol{B}_s$ is caused by the Pauli spin paramagnetism of the conduction electrons: $\boldsymbol{B}_s = A_s \chi_s \boldsymbol{H}_{ext}$, where χ_s is the isotropic and temperature-independent Pauli spin susceptibility. Equation (2) can now be written as

$$K = \frac{1}{H_{ext}^2} \boldsymbol{H}_{ext} (A_0 \boldsymbol{\chi}_f + \mathbf{A}_{dip} \boldsymbol{\chi}_f) \boldsymbol{H}_{ext} + K_s \tag{6}$$

where $K_s = A_s \chi_s$ is the Pauli contribution. The susceptibility tensor $\boldsymbol{\chi}_f$ in equations (1), (4), (5) and (6) is understood to be an atomic susceptibility (emu/U ion). If all U ions were to carry the same $\boldsymbol{\chi}_f$, it could be related to the measured bulk susceptibility by

$$\boldsymbol{\chi}_b = N_A \boldsymbol{\chi}_f \qquad \text{(emu/mol U)} \tag{7}$$

where N_A is Avogadro's number (we neglect here the small contribution of χ_s). The above assumption is questionable in view of the presence of three magnetically inequivalent U ions. More appropriately we should write

$$\boldsymbol{\chi}_b = \frac{1}{14} N_A (6\boldsymbol{\chi}_{\mathrm{U1}} + 6\boldsymbol{\chi}_{\mathrm{U2}} + 2\boldsymbol{\chi}_{\mathrm{U3}}) \qquad \text{(emu/mol U)} \tag{8}$$

and equations (4), (5) and (6) have then to be modified accordingly. The measured bulk susceptibility is well described by a Curie–Weiss law down to nearly T_N (see table 1). The Curie constant C and the effective moment p_{eff} are derived by assuming that C and p_{eff}, respectively, are the same for all U ions. Assuming that $p_{eff} = 0$ for the U3 ions, the U1 and U2 ions together would show an average p_{eff} which is larger by 8% than the values in table 1 and would shift the values closer to the Hund's rule values of 3.58 and 3.62 for U^{3+} and U^{4+}, respectively. However, this is not a sufficient argument in favour of $p_{eff}(\mathrm{U3}) = 0$.

Directing the external field along one of the principal axes of the susceptibility tensor ($\boldsymbol{a}, \boldsymbol{b}^*, \boldsymbol{c}$) equation (6) may be rewritten as follows:

$$\begin{aligned} K_a &= (A_0 + A_{aa}^{dip})\chi_a + K_s \\ K_{b^*} &= (A_0 + A_{b^*b^*}^{dip})\chi_{b^*} + K_s \\ K_c &= (A_0 + A_{cc}^{dip})\chi_c + K_s \end{aligned} \tag{9}$$

with $\mathrm{Tr}\,\mathbf{A}_{dip} = 0$. From the bulk susceptibility it follows that $\chi_a = \chi_{b^*} = \chi_\perp$, which reflects the axial symmetry of the hexagonal lattice. However, at the atomic level, χ_a may be different from χ_{b^*}, as may be deduced from inspection of figure 1 by considering just one of the triangles formed by the U1 or U2 ions. For later use we also write down the full angular dependence of K when the external field is rotated in the $\boldsymbol{a}$–$\boldsymbol{b}^*$ plane:

$$\begin{aligned} K(\varphi) = (A_0 + A_{b^*b^*}^{dip})\chi_{b^*} + ((A_{aa}^{dip} + A_0)\chi_a - (A_{b^*b^*}^{dip} + A_0)\chi_{b^*})\cos^2\varphi \\ + \frac{1}{2} A_{ab^*}^{dip} (\chi_{b^*} + \chi_a) \sin 2\varphi. \end{aligned} \tag{10}$$

φ is the angle between $\boldsymbol{H}_{ext}$ and the a-axis. In the case of a diagonal $\mathbf{A}_{dip}$, $K(\varphi)$ will assume an extremum at $\varphi = 0$; otherwise, the extremum will be shifted to some non-zero φ.

Rotating the field in the a–c plane ($\varphi = 0$), one derives instead

$$K(\vartheta) = (A_0 + A_{aa}^{dip})\chi_a + ((A_{cc}^{dip} + A_0)\chi_c - (A_{aa}^{dip} + A_0)\chi_a)\cos^2\vartheta + \frac{1}{2}A_{ac}^{dip}(\chi_a + \chi_c)\sin 2\vartheta. \tag{11}$$

ϑ is the angle between $\boldsymbol{H}_{ext}$ and the c-axis.

So far we have neglected macroscopic contributions to the frequency shift which arise from the magnetization of the sample, namely the demagnetization field $\boldsymbol{B}_{dm}$ and the Lorentz field $\boldsymbol{B}_L$. Explicitly, we have

$$\boldsymbol{B}_{dm} = -\mathbf{N}\boldsymbol{\chi}_b^*\boldsymbol{H}_{ext} \tag{12}$$

$$\boldsymbol{B}_L = \frac{4\pi}{3}\boldsymbol{\chi}_b^*\boldsymbol{H}_{ext} \tag{13}$$

where $\mathbf{N}$ is the demagnetization factor (tensor) which depends on the shape of the sample and $\boldsymbol{\chi}_b^*$ is now the magnetic bulk susceptibility per unit volume, i.e. $\boldsymbol{\chi}_b^* = (\rho/M)\boldsymbol{\chi}_b$ (emu cm^{-3}). In the present case the principal axes of $\mathbf{N}$ agree with the crystallographic axes; i.e. $\mathbf{N}$ is diagonal in the system $\boldsymbol{a}, \boldsymbol{b}^*, \boldsymbol{c}$ (see table 2).

The total relative frequency shift $\Delta\nu/\nu_0$ has to be corrected for these additional shifts to arrive at the true Knight shift, i.e.

$$K_i = \frac{\Delta\nu_i}{\nu_0} - \frac{\rho}{M}\left(\frac{4\pi}{3} - N_{ii}\right)\chi_i \qquad (i = a, b^*, c). \tag{14}$$

The relevant N_{ii} for the samples used in this work are listed in table 2.

3.2. Experimental results

The transverse-field (TF) μSR signal [4] showed in general a splitting into four components. In addition, a more or less intense background signal was seen from μ^+ stopping outside of the sample. As an example, figure 2 shows the Fourier transform (power) of the μSR signal taken at 80 K for sample No 3 in the GPS. The dominant peak arises from two overlapping

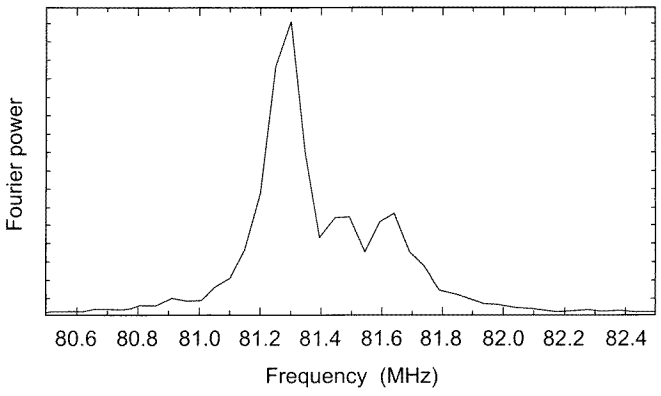

Figure 2. The Fourier power spectrum of the TF μSR signal ($H_{ext} = 6$ kOe) taken at 80 K with $\boldsymbol{H}_{ext}$ applied in the a–b plane. The dominant peak consists of two components, as follows from the actual fit of the original μSR spectrum.

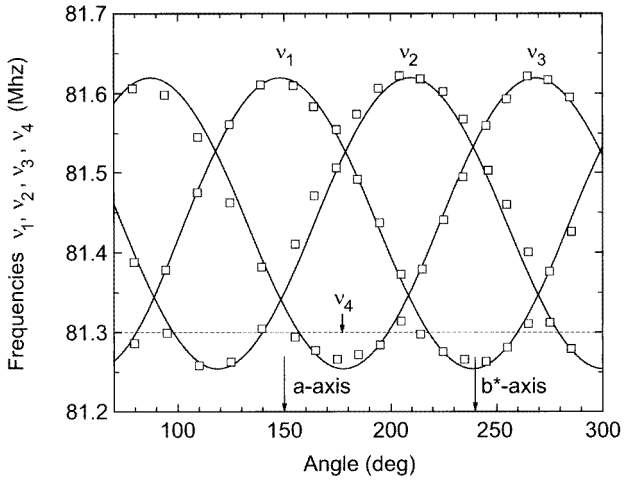

Figure 3. The dependence of the precession frequencies ν_1, ν_2 and ν_3 on the orientation of the field $\boldsymbol{H}_{ext}$ applied in the basal a–b plane at 80 K. ν_4 is represented by the horizontal line.

components. (The background signal was negligibly small in this measurement.) Although they cannot be resolved in the Fourier spectrum, they can be fitted in the time domain by imposing constraints on the amplitudes—namely that three out of the four components displayed the same signal amplitude. These three components (labelled No 1, No 2 and No 3) showed a striking angular dependence of the precession frequencies when the external field $\boldsymbol{H}_{ext}$ was rotated in the basal plane, i.e. when the sample was rotated around the c-axis (in this case the demagnetization factor N was constant; see table 2). The results are displayed in figure 3. The solid lines are $\cos^2\varphi$ fits. As can be seen, the lines are displaced from each other by 60°. This is what one would expect, if three magnetically inequivalent but crystallographically equivalent μ^+-positions are assumed which can be transformed

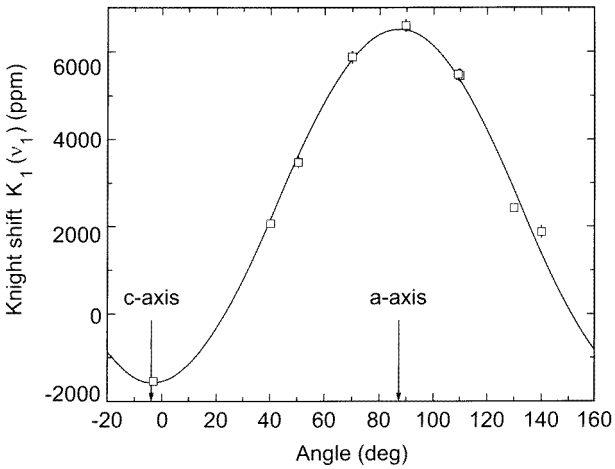

Figure 4. The dependence of the Knight shift derived from precession component No 1 on the orientation of $\boldsymbol{H}_{ext}$ in the a–c plane at 30 K.

into each other by rotations of 120° around the c-axis. The maximum frequency shift was observed when $\boldsymbol{H}_{ext}$ was parallel to the crystallographic a-axis or equivalent directions. From comparison with equation (10), it follows that $A^{dip}_{ab^*}$ must be zero or quite small.

When the external field was directed along the c-axis, the three frequency shifts coalesced into one and assumed a minimum, as can be seen from figure 4 which displays the angular dependence of the Knight shift of component No 1 in the a–c plane. Again, from comparison with equation (11), it follows that $A^{dip}_{ac} \simeq A^{dip}_{b^*c} \simeq 0$.

These results already allow us to predict that the three sites involved are most likely to be found in the U1- or U2-containing planes ($z = 1/2$, $z = 0$).

The fourth single component (labelled No 4) shows no angular dependence in the basal plane. Some anisotropy with respect to the c-axis is not yet totally excluded, but if there is any, it must be rather small. In any case the associated μ^+-position must be essentially a magnetically (and of course crystallographically) unique position.

In order to actually determine the full $\mathbf{A}_{dip}$ tensor, the temperature dependences of the Knight shifts were studied for $\boldsymbol{H}_{ext} \parallel a$-axis, $\boldsymbol{H}_{ext} \parallel b^*$-axis and $\boldsymbol{H}_{ext} \parallel c$-axis. Fig-

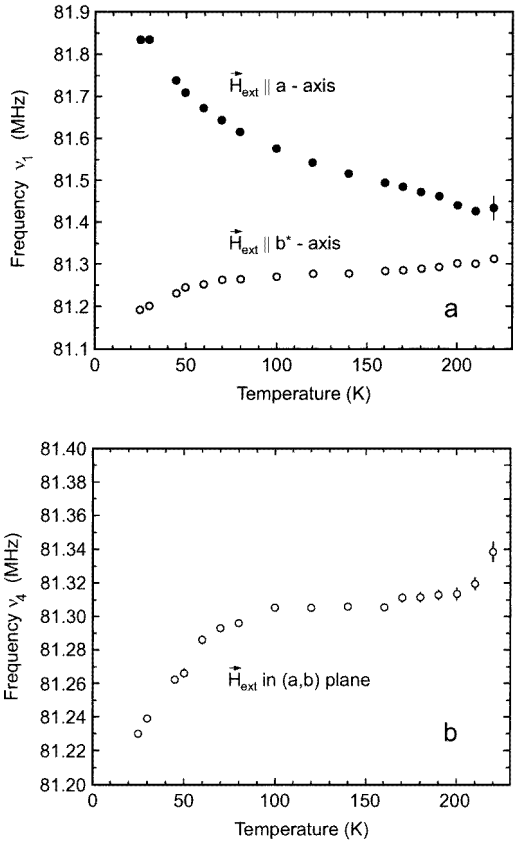

Figure 5. (a) The temperature dependence of the precession frequency ν_1 for $\boldsymbol{H}_{ext} \parallel a$-axis and for $\boldsymbol{H}_{ext} \parallel b^*$-axis. Above 180 K the two frequencies start to approach each other, which signals the onset of μ^+-diffusions among the sites I. (b) The temperature dependence of the precession frequency ν_4 (component No 4). The upturn of ν_4 at 220 K signals the onset of long-range μ^+-diffusion involving sites I and II.

ure 5(a) displays the temperature dependence of the uncorrected frequencies associated with the maximum ($\boldsymbol{H}_{ext} \parallel a$-axis) and the minimum ($\boldsymbol{H}_{ext} \parallel b^*$-axis) in figure 3. We find that the two frequencies start to approach each other above 180 K, and above 220 K only one component remains. This behaviour reflects the onset of μ^+-diffusion (motional averaging). The analysis of the data was therefore restricted to temperatures below 180 K, except for $\boldsymbol{H}_{ext} \parallel c$-axis in which case diffusion does not matter in view of the degeneracy of the frequency shifts. Figure 5(b) shows the temperature dependence of the frequency of component No 4.

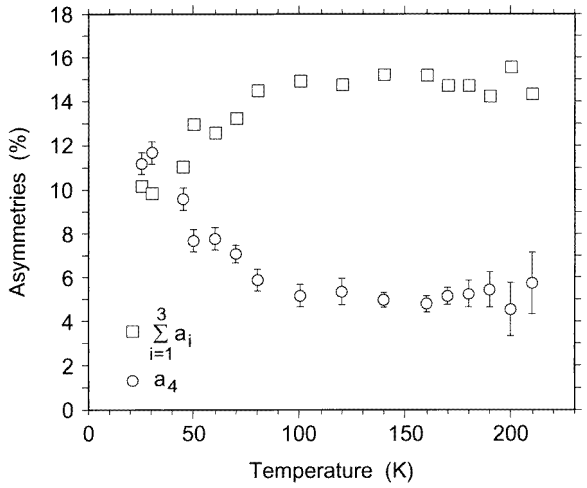

Figure 6. The temperature dependence of the total asymmetries (signal amplitudes) of the site-I and site-II signals.

The relative population of the site associated with components No 1, No 2, No 3 (henceforth labelled site I) and the site associated with component No 4 (henceforth labelled site II) is temperature dependent. Figure 6 displays the temperature dependence of the sum of the amplitudes of components No 1–No 3 and the amplitude of component No 4 measured for sample No 3. The amplitudes are a direct measure of the relative populations. As can be seen, close to T_N the population of the two sites is nearly equal but the population $P(\mathrm{I})$ of site I grows at the expense of the population $P(\mathrm{II})$ of site II. This feature is generally seen for all three samples, but the ratio $P(\mathrm{I})/P(\mathrm{II})$ may deviate in either direction from the value quoted above, depending on the sample used. These discrepancies are not understood at present.

Each precession component appears to relax exponentially. The relaxation rate of component No 4 is the smallest and drops above 30 K to rates below 0.05 μs^{-1}. The relaxation rates of the other components assume a maximum for the maximum frequency shift ($\simeq$0.6 μs^{-1} at 25 K) but drop quickly with rising temperature, always staying below 0.2 μs^{-1} above 50 K. These results will not be discussed further here.

3.3. Analysis of the Knight shift data

All of the measured frequency shifts were corrected for the demagnetization and Lorentz contributions using the demagnetization factors listed in table 2 and the bulk susceptibility from reference [3], which was measured for a sample cut from the same large crystal as the

Table 3. A collection of fitted parameters of site-I components (No 1, No 2, No 3).

	a-axis	*b**-axis	*c*-axis
$A_{ii}C$ (K)	0.622(37)	$-(1.34 \pm 0.55) \times 10^{-2}$	$-0.407^{+0.110}_{-0.182}$
A_{ii} (kG/μ_B)	2.80 ± 0.17†	-0.060 ± 0.025†	$-1.83^{+0.49\dagger}_{-0.82}$
A_{ii} (kG/μ_B)	2.40 ± 0.14‡	-0.052 ± 0.021‡	$-1.57^{+0.42\ddagger}_{-0.70}$
K_i^0 (ppm)	-475 ± 140	-272 ± 35	513^{+309}_{-227}
θ_i' (K)	-57 ± 3	$+13 \pm 2$	-164^{+37}_{-53}

† Calculated with $C = 1.241$ emu K/mol U ($p_{eff} = 3.15$, averaged from reference [3]; see table 1).
‡ Calculated with $C = 1.447$ emu K/mol U ($p_{eff} = 3.40$, assuming that $p_{eff}(\mathrm{U3}) = 0$).

Table 4. A collection of fitted parameters of the site-II component (No 4).

	a–*b* plane	*c*-axis
$A_{ii}C$ (K)	$-(1.03 \pm 0.55) \times 10^{-2}$	$-(1.05^{+0.33}_{-0.46}) \times 10^{-2}$
A_{ii} (kG/μ_B)	-0.046 ± 0.025†	$-0.047^{+0.15\dagger}_{-0.21}$
K_i (ppm)	$+200 \pm 50$	+300 fixed
θ_i' (K)	11.4 ± 2.4	26^{+12}_{-19}

† Calculated with $C = 1.241$ emu K/mol U ($p_{eff} = 3.15$); the values will be reduced by ∼17% if $C = 1.447$ emu K/mol U ($p_{eff}(U3) = 0$) is used.

present samples No 1–No 3.

Inspection of the corrected Knight shifts as a function of temperature showed that they followed a Curie–Weiss behaviour from 180 K down to ∼30 K. Consequently they were fitted using the function

$$K_i = K_i^0 + A_{ii}\frac{C}{T + \Theta_i'} \tag{15}$$

where

$$C = \frac{P_{eff}^2 \mu_B^2}{3k_B}$$

is the Curie constant/U ion and

$$p_{eff} = \sqrt{J(J+1)}g_J$$

is the effective moment (in units of μ_B). The latter may be taken from table 1, or, if the U3 ions are magnetically inactive, has to be increased by $\sqrt{(14/12)}$ or 8%, respectively. K_i^0 is a temperature-independent term which may be identified with K_s (equation (9)); $A_{ii} = A_0 + A_{ii}^{dip}$ are the coupling constants defined in section 3.1 and θ_i' is an effective Curie–Weiss temperature. The fitting parameters are collected in tables 3 and 4; θ_i' is also given in table 1 for comparison. Figure 7 shows a Curie plot of $(K_i(T) - K_i^0)^{-1}$ versus temperature for the site-I results.

The data for different samples, involving different demagnetization factors and different external fields, resulted in coinciding parameter sets, proving the consistency of our analysis.

A most unexpected result is that the effective Curie–Weiss temperatures are quite different from the values deduced from the bulk susceptibility (see table 1), even showing an

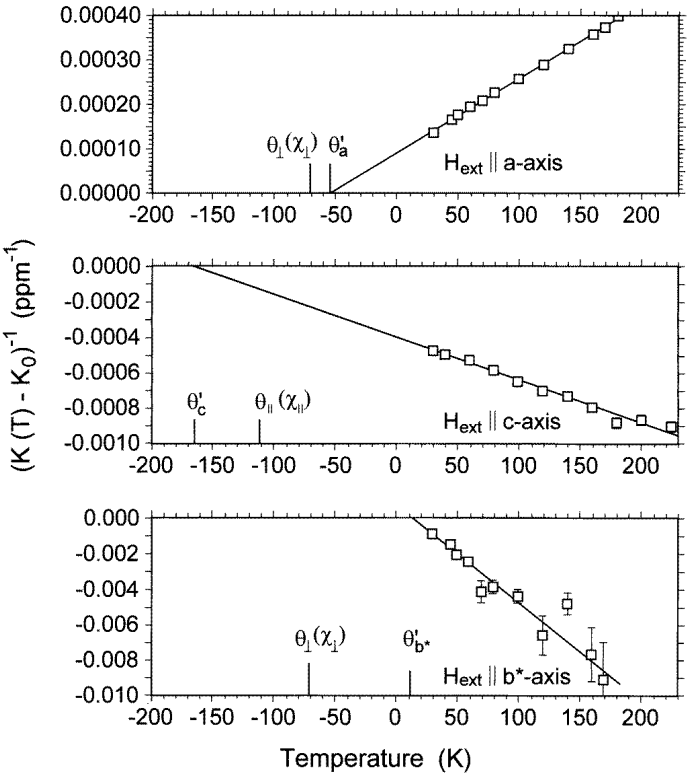

Figure 7. Curie–Weiss plots of $(K_i(T)-K_0)^{-1}$ versus temperature. Note the shifted positions of the Curie–Weiss temperatures θ_i' with respect to $\theta_\perp$ and $\theta_\parallel$ deduced from the bulk susceptibility.

anisotropy in the basal plane. Also unusual is the anisotropy of the temperature-independent contribution K_s. Note that A_{cc} is the least accurately determined coupling constant.

Table 5. Hyperfine coupling constants for site I.

		a-axis	b^*-axis	*c*-axis
$p_{eff} = 3.15$	A_{ii}^{dip} (kG/μ_B)	$2.50^{+0.18}_{-0.28}$	$-0.36^{+0.17}_{-0.29}$	$-2.13^{+0.25}_{-0.41}$
	A_0 (kG/μ_B)		$0.30^{+0.17}_{-0.28}$	
$p_{eff} = 3.40$	A_{ii}^{dip} (kG/μ_B)	$2.14^{+0.15}_{-0.25}$	$-0.31^{+0.15}_{-0.24}$	$-1.93^{+0.20}_{-0.33}$
(see table 3)	A_0 (kG/μ_B)		$0.26^{+0.15}_{-0.24}$	

From the A_{ii}-values in tables 3 and 4 we can now deduce the dipolar coupling tensor $\mathbf{A}_{dip}$ and the contact coupling constant A_0, making use of the additional constraint that $\mathrm{Tr}\,\mathbf{A}_{dip} = 0$. The values obtained pertaining to site I are listed in table 5. For site II, only a contact coupling constant can be extracted: $A_0 = -0.040 \pm 0.021$ kG/μ_B, while any non-zero A_{ii}^{dip} is restricted to $|A_{ii}^{dip}| \lesssim |A_0|$. Compared to the values for site I, all A_0, A_{ii}^{dip} are extremely small, while $|K_s|$ is of similar magnitude.

3.4. Identification of μ^+-sites

The identification proceeds as follows: we first calculate the tensor $\mathbf{A}_{dip}$ by performing the appropriate lattice summation (equation (3)), scanning the crystal (i.e. the $z = 0$ and $z = 1/2$ planes) in steps of $0.01a$ and $0.02b$ (using the crystal parameters of reference [3]). We then diagonalize $\mathbf{A}_{dip}$ since the measured $\mathbf{A}_{dip}$ is in a diagonal form. Next we produce contour plots of the diagonalized A_{ii}^{dip} and search for those contour lines which agree with the measured $A_{ii}^{dip} \pm$ error bars. If those A_{aa}^{dip}-, $A_{b^*b^*}^{dip}$- and A_{cc}^{dip}-lines cross simultaneously at the same position, this position qualifies as a possible μ^+-site.

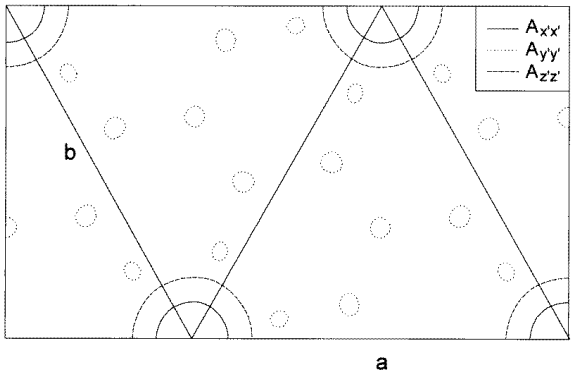

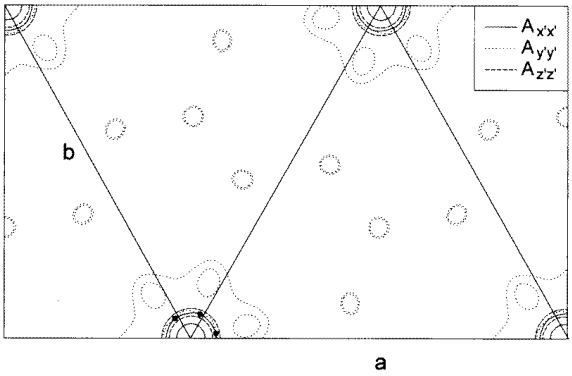

Figure 8. Calculated contour lines for $A_{ii}^{dip} = 0$ (upper part) and $A_{ii}^{dip} = \pm 50$ G/μ_B (lower part) in the $z = \frac{1}{2}$ plane. In the upper part p_{eff}(U3) $= p_{eff}$(U1); in the lower part p_{eff}(U3) $= 0.08 p_{eff}$(U1). The black dots in the lower part indicate the points where the A_{ii}^{dip} overlap within their error bars. The axes x', y', z' are the principal axes of the tensor $\mathbf{A}_{dip}$ and vary as a function of position.

We first consider the site-II position. The smallness of the coupling constants implies a position which is either far from the U ions or near a point where the dipole and contact fields from the various U ions cancel each other. Assuming that the U3 ions are magnetically inactive (p_{eff}(U3) $= 0$), calculations of A_{ii}^{dip} in the $z = 0$ and $z = \frac{1}{2}$ planes (using the crystal parameters of reference [3]) show generally that $|A_{cc}^{dip}| > 0.2$ kG/μ_B, which is incompatible with the data. Also, inspection of the crystal shows that in between the

$z = 0$ and $z = \frac{1}{2}$ planes no reasonable interstitial site can be identified. The situation is different if the U3 ions are allowed to show a magnetic response, i.e. $p_{eff}(\mathrm{U3}) \neq 0$. Assuming first that $p_{eff}(\mathrm{U3}) = p_{eff}(\mathrm{U1}) = p_{eff}(\mathrm{U2})$, we calculate again A_{ii}^{dip}-maps in the $z = 0$ and $z = \frac{1}{2}$ planes. The upper part of figure 8 displays the resulting contour lines for $A_{aa}^{dip} = A_{b^*b^*}^{dip} = A_{cc}^{dip} = 0$ kG/μ_B in the $z = \frac{1}{2}$ plane. A similar plot is obtained for the $z = 0$ plane. As can be seen, we now do indeed find lines with $A_{ii}^{dip} = 0$ for all ii, but they do not cross at any position. On reducing $p_{eff}(\mathrm{U3})$, all zero lines (except certain $A_{b^*b^*}^{dip}$-lines) move towards the position (0 0 $\frac{1}{2}$) or equivalent ones, starting to overlap for $p_{eff}(\mathrm{U3}) \lesssim 0.1 p_{eff}(\mathrm{U1, U2})$ and shrinking to the position (0 0 $\frac{1}{2}$) for $p_{eff}(\mathrm{U3}) = 4.14 \times 10^{-2} p_{eff}(\mathrm{U1, U2})$. The $A_{ii}^{dip} = 0 \pm 50$ G/μ_B contour lines for $p_{eff}(\mathrm{U3}) = 0.08 p_{eff}(\mathrm{U1, 2})$ are displayed in the lower part of figure 8. A similar behaviour is also found in the $z = 0$ plane, now involving the position (0 0 0). We conclude that site II is located in the vicinity of position (0 0 0) or (0 0 $\frac{1}{2}$). However, inspection of the atomic environment of position (0 0 0) reveals that the nearest-neighbour Au ions (Au5), in the $z = 0$ plane, are at a distance of only 1.3 Å. Moreover, there are twice as many $6j$-positions as there are Au5 ions and the Au5 ions are randomly distributed over the $6j$-sites, so on average each $6j$-site has an occupation probability of only 50%. This introduces a certain randomness in the atomic configuration around the (0 0 0) position. In view of this, we believe that site II cannot be located near the (0 0 0) position. In contrast, the interstitial volume at the position (0 0 $\frac{1}{2}$) is much larger: the distance to the nearest U3 ion amounts to 1.8 Å and the six nearest Au4 ions in the $z = \frac{1}{2}$ plane are at a distance of ∼2.9 Å. Our final conclusion, therefore, is that site II is located in the $z = \frac{1}{2}$ plane close to the position (0 0 $\frac{1}{2}$), i.e. halfway between the pair of U3 ions forming together a nearly non-magnetic configuration. As figure 8 demonstrates, the possible μ^+-sites, compatible with the calculated $A_{ii}^{dip} = 0$, are again of threefold (sixfold) symmetry. Because $A_{ii}^{dip} \simeq 0$, the sites are indistinguishable from each other.

The present analysis shows that the results on the site-II signal can only be explained if one admits a non-zero magnetic response of the U3 ions, but with a rather reduced $p_{eff}(\mathrm{U3})$ within the limits $4.13 \times 10^{-2} \leqslant p_{eff}(\mathrm{U3})/p_{eff}(\mathrm{U1, 2}) < 0.1$.

Next we consider the location of site I. The fact that $A_{b^*c}^{dip}$, A_{ac}^{dip} must be quite small in view of figure 4 leads us to suspect that in fact $A_{b^*c}^{dip} = A_{ac}^{dip} \equiv 0$. This situation is generally found for the $z = 0$ and $z = \frac{1}{2}$ planes, containing either the U2 or the U1 ions, respectively. Again we have calculated the spatial dependence of the diagonalized $\mathbf{A}_{dip}$ in the $z = 0$ and $z = \frac{1}{2}$ planes, assuming from now on that $p_{eff}(\mathrm{U3}) = 0$ and $p_{eff}(\mathrm{U1}) = p_{eff}(\mathrm{U2})$ (admitting a $p_{eff}(\mathrm{U3}) \lesssim 0.1 p_{eff}(\mathrm{U1, 2})$ has a negligible effect on the following conclusions). The diagonalization allows us also to determine the angle α between the principal axes (x', y') of $\mathbf{A}_{dip}$ in the basal plane and the laboratory axes (x, y) defined by the crystallographic a- and b^*-axes (the z'- and c-axis will be parallel). Figures 9 and 10 display contour lines of A_{ii}^{dip} in the $z = \frac{1}{2}$ and $z = 0$ planes respectively, for values plus or minus the error bars taken from table 5, lower part. Also shown are contour lines corresponding to $\alpha = 0^\circ$, (i.e. $A_{ab^*}^{dip} = 0$; this applies to signal No 1). The contour lines for $\alpha = \pm 120^\circ$ (equivalent to $\mp 60^\circ$, associated with signals No 2 and 3) (not shown for clarity) can be obtained by rotating the pattern by $\pm 120^\circ$. Possible μ^+-sites are again those regions in which the A_{aa}^{dip}-, $A_{b^*b^*}^{dip}$-, A_{cc}^{dip}- and $\alpha = 0, \pm 120^\circ$ lines cross simultaneously. We find that there are several sets of three symmetrically coordinated candidate sites in the $z = \frac{1}{2}$ plane (indicated by •; only the sites with $\alpha = 0^\circ$ are marked; the symmetrically coordinated sites with $\alpha = \pm 120^\circ$ are not shown).

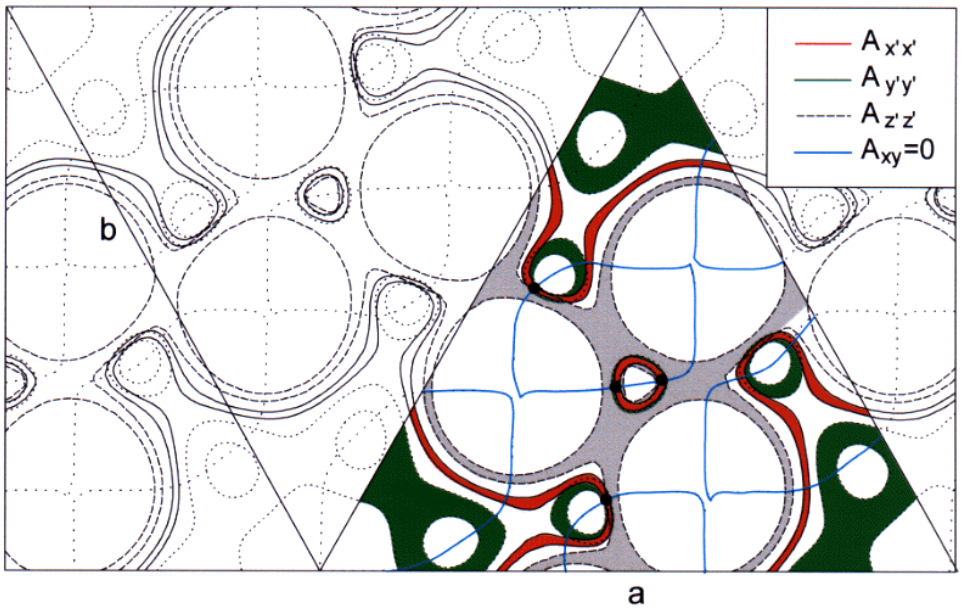

Figure 9. Calculated contour lines for the principal-axis values $A^{dip}_{x'x'}$, $A^{dip}_{y'y'}$, $A^{dip}_{z'z'}$ and (blue line) $A^{dip}_{xy} = 0$ (corresponding to $\alpha = 0^\circ$) in the $z = \frac{1}{2}$ plane with $A^{dip}_{i'i'}$ equal to the experimental values plus or minus the error bars (table 3; p_{eff}(U3) = 0). To make the illustration clearer, the area between the $A^{dip}_{i'i'} \pm \Delta A^{dip}_{i'i'}$ lines is coloured in part of the plot (red: A^{dip}_{aa}; green: $A^{dip}_{b^*b^*}$; grey: A^{dip}_{cc}). Possible μ^+-sites are those positions where the (coloured) stripes, formed by the corresponding contour lines plus the $\alpha = 0^\circ$ line, all overlap. These sites are marked by •. If we included also the $\alpha = \pm 120^\circ$ contour lines (not shown for clarity), the number of possible sites would triple.

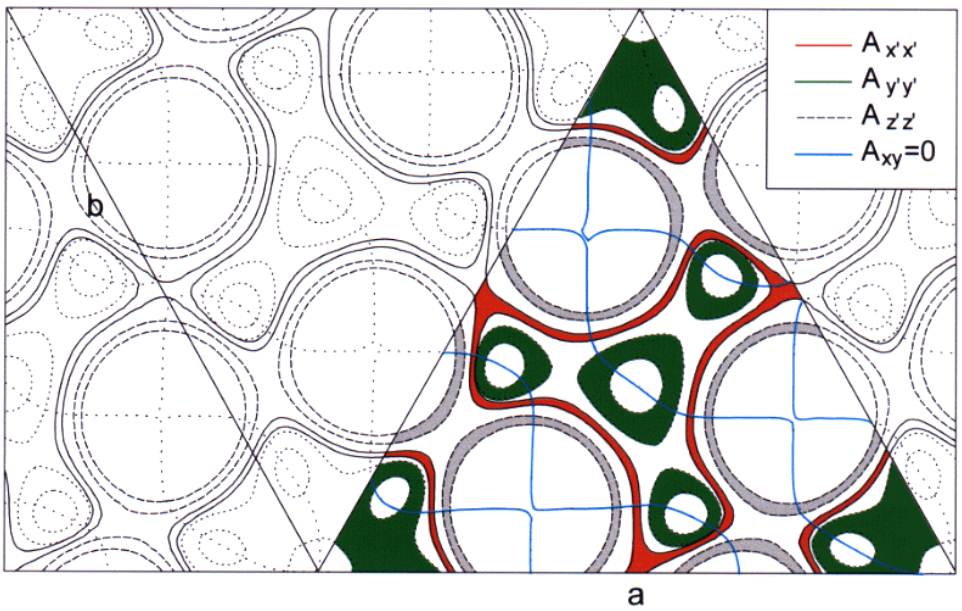

Figure 10. Calculated contour lines in the $z = 0$ plane. See the caption of figure 9.

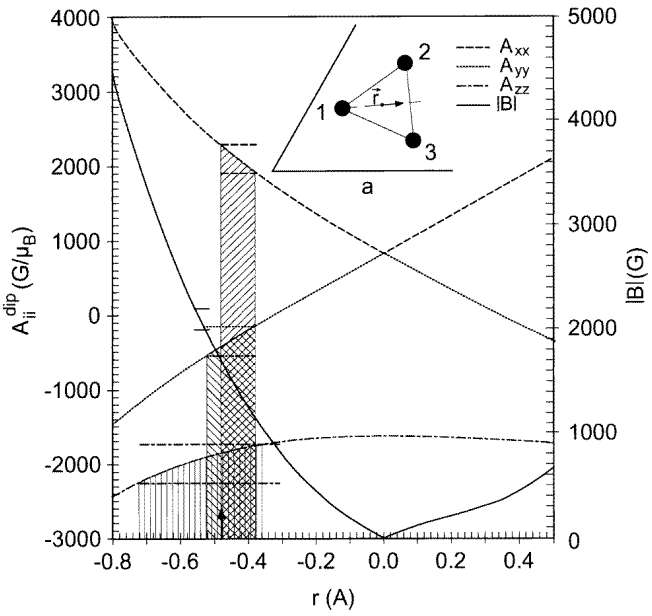

Figure 11. The calculated diagonalized $A^{dip}_{x'x'}$, $A^{dip}_{y'y'}$ and A^{dip}_{cc} along the line shown in the inset. The position $r = 0$ refers to the centre of the triangle. Also shown are dipolar fields calculated according to section 4.2 (solid line). This line will be pushed up when the contact field $\boldsymbol{B}_c$ is added to $\boldsymbol{B}_{dip}$. The vertical lines indicated represent the measured A^{dip}_{ii} and $|\boldsymbol{B}_1|$ plus or minus their error bars. The approximate centre of the overlapping ranges of μ^+-positions is indicated by the arrow. Note the almost perfect consistency with the measured $|\boldsymbol{B}_1|$.

We rule out those sites which possess a fully asymmetric configuration of the nearest-neighbour U1 ions and Au ions. This leaves us with only one possible set near the centre of an even-sided U1 triangle. An individual site of this set is located on the connecting straight line between a U1 ion and the centre of the triangle. Note that the other site indicated, on the opposite side of the centre, involves an asymmetric neighbour configuration.

Examining figure 10, we do not find any position in the $z = 0$ plane at which the allowed ranges of the $A^{dip}_{i'i'}$ and α cross simultaneously, ruling out a μ^+-site in the $z = 0$ plane.

The coordinates of one of the three site-I candidates are read off figure 11, which shows the dependence of the diagonalized $A^{dip}_{x'x'}$, $A^{dip}_{y'y'}$, A^{dip}_{zz} on the position along the line between the U1 atom No 1 (see figure 1) and the centre of the U1 triangle at $(\frac{2}{3}\ \frac{1}{3}\ \frac{1}{2})$. Also indicated are the experimental results and their error bars. The experimental values cross the calculated values approximately at the position (0.63(1) 0.3319(5) 0.5). The other sites are obtained by proper symmetry operations.

Figure 12 shows the atomic configuration around this site. The nearest neighbours out of the $z = \frac{1}{2}$ plane are the gold ions Au6 at the positions (0.666, 0.333, 0.500 ± 0.191). The distances are indicated in the figure. The nearest neighbours perpendicular to the U1–Au6–Au6 plane are four gold ions Au3 in a rectangular planar array.

The three site-I positions are quite close (distance ≈ 0.79 Å). Therefore, the onset of μ^+-diffusion at around 180 K may initially only reflect a local hopping between these three sites, while long-range diffusion also involving site II may become effective above 210 K.

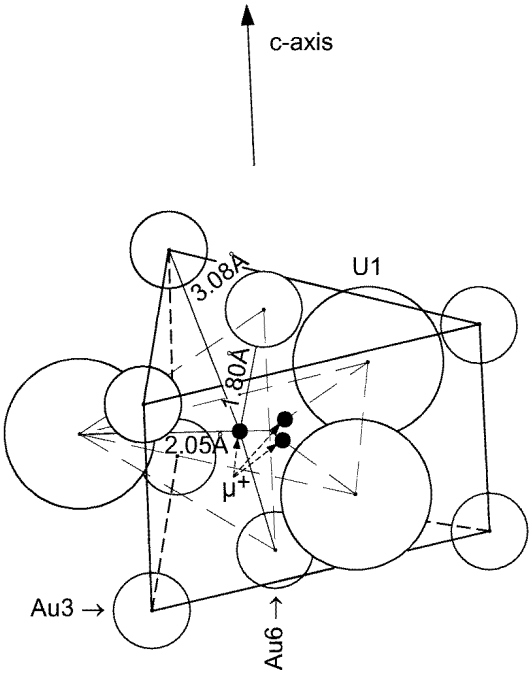

Figure 12. The nearest-neighbour configuration consisting of three U1 atoms, two Au6 atoms and six Au3 atoms around site I. As indicated, there are three crystallographically equivalent positions.

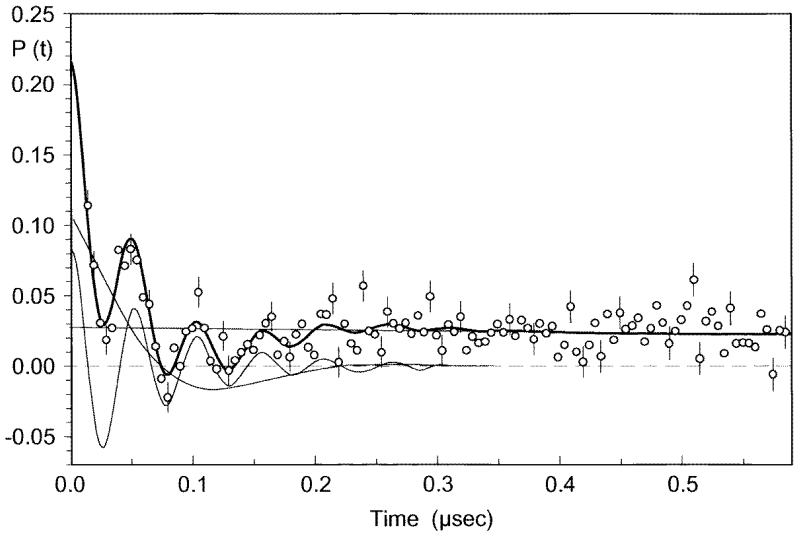

Figure 13. The ZF μSR signal at 19 K for the magnetically ordered state of $U_{14}Au_{51}$. The solid line represents a fit of equation (16) to the data. The initial polarization $\boldsymbol{P}_\mu(0)$ was roughly parallel to the *c*-axis.

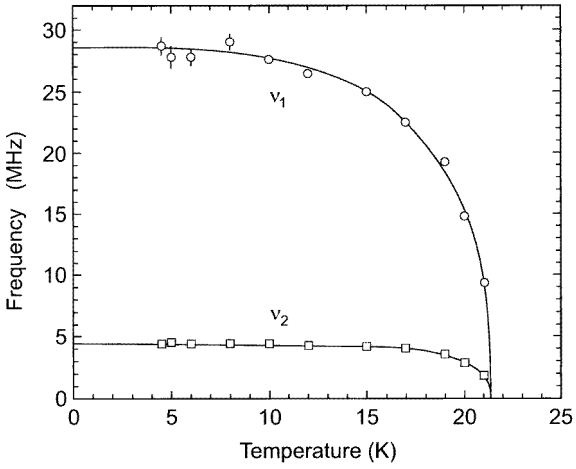

Figure 14. The temperature dependences of the spontaneous frequencies ν_1 and ν_2. The solid lines represent fits of equation (18) to the data.

4. Measurements for the magnetically ordered state

4.1. Results

A typical ZF μSR signal below T_N is shown in figure 13. The time evolution of the μ^+-polarization contains three components, and is best fitted by the function

$$P(t) = a_1 e^{\lambda_1 t} \cos \omega_1 t + a_2 e^{-\lambda_2 t} \cos \omega_2 t + a_3 e^{-\lambda_3 t}. \tag{16}$$

Other assumptions regarding the form of $P(t)$ proved to be less satisfactory. Two components thus reflect the μ^+ Larmor precession in two different spontaneous internal fields $B_i = \omega_i/\gamma_\mu$ as expected in the presence of two different types of μ^+-site. The

Table 6. A list of the fitting values (equation (17)) for describing $B_i(T)$ and the theoretical predictions. (MF = mean field.)

Signal	ν_0 (MHz)	B_0 (kG)	δ	β	T_N (K)
Site II	4.41 ± 0.05	0.325 ± 0.040	$5.23^{+1.97}_{-1.40}$	$0.31^{+0.16}_{-0.08}$	$21.22^{+0.27}_{-0.12}$
Site I	28.50 ± 0.36	2.102 ± 0.027	3.13 ± 0.40	0.34 ± 0.03	21.25 ± 0.06
I_{ns} (110) (reference [3])			4.2 ± 0.1	0.398 ± 0.014	21.64 ± 0.04
MF				0.5	
Heisenberg $D = 3$				 0.38	
Ising $D = 2$ (reference [8]) $D = 3$				 0.125 0.312	
χ (reference [3])					21.3(2) (c-axis) 22.0(2) (b-axis)

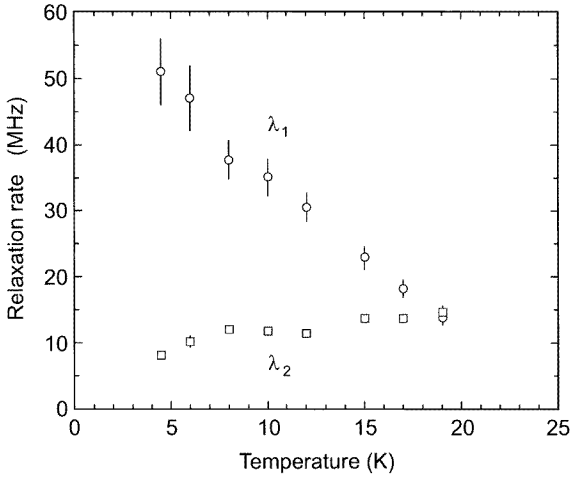

Figure 15. The temperature dependences of the relaxation rates λ_1 and λ_2.

temperature dependences of the fitted frequencies are displayed in figure 14. The low-temperature limits of $\nu_1 = 29.5$ MHz and $\nu_2 = 4.40$ MHz correspond to internal fields of 2.10 kG and 0.325 kG (see also table 6). The temperature dependences of λ_1 and λ_2 are displayed in figure 15. We notice that the ratio λ_1/λ_2 is close to $\nu_1/\nu_2 \simeq 6.7$ at 4.5 K, but approaches 1 for $T \rightarrow T_N$, in contrast to the behaviour of ν_1/ν_2 (see the next section). λ_3 appears to be temperature independent, and has a value of $\sim 0.3\ \mu s^{-1}$.

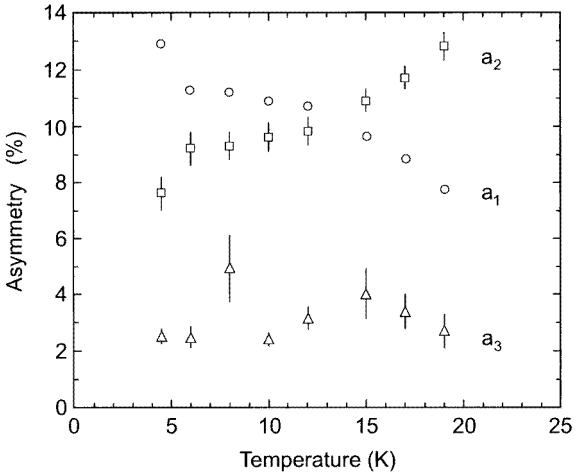

Figure 16. The temperature dependences of the amplitudes (asymmetries) a_1, a_2 and a_3 (equation (16)). The orientation of $\boldsymbol{P}_\mu(0)$ is like that in figure 14.

The temperature dependences of the asymmetries or amplitudes a_i are displayed in figure 16. The non-oscillating a_3 is rather small ($\sim$10% of the total asymmetry) and is moreover temperature independent. The sum $a_1 + a_2 + a_3$ adds up to the possible maximum value, which is given by the projection of the initial μ^+-polarization $\boldsymbol{P}_\mu(0)$ onto the direction of positron observation, i.e. there is no missing polarization. Hence it appears

that almost the full $\boldsymbol{P}_\mu(0)$ is precessing. This implies that the internal fields $\boldsymbol{B}_i$ 'sensed' by the μ^+ are oriented nearly perpendicular to $\boldsymbol{P}_\mu(0)$, i.e. that the μ^+-spin precession is essentially of planar geometry. Since the experimental arrangement was such that $\boldsymbol{P}_\mu(0)$ was roughly directed perpendicular to the crystalline *a–b* plane, it follows that the $\boldsymbol{B}_i$ are likewise confined to the *a–b* plane. We will see that this is precisely what would be expected on the basis of the μ^+-site determinations and the AF structure of reference [3]. The small non-oscillating component a_3 may indicate a certain misalignment ($\sim 20^\circ$), so in fact $\boldsymbol{P}_\mu(0)$ may not be exactly perpendicular to the $\boldsymbol{B}_i$. It is also possible that this component arises from a small fraction of the sample volume which has remained paramagnetic below T_N.

The amplitudes a_1 and a_2 reveal a certain temperature dependence which seems to imply that even below T_N the relative population of the two sites is not constant (see the discussion below).

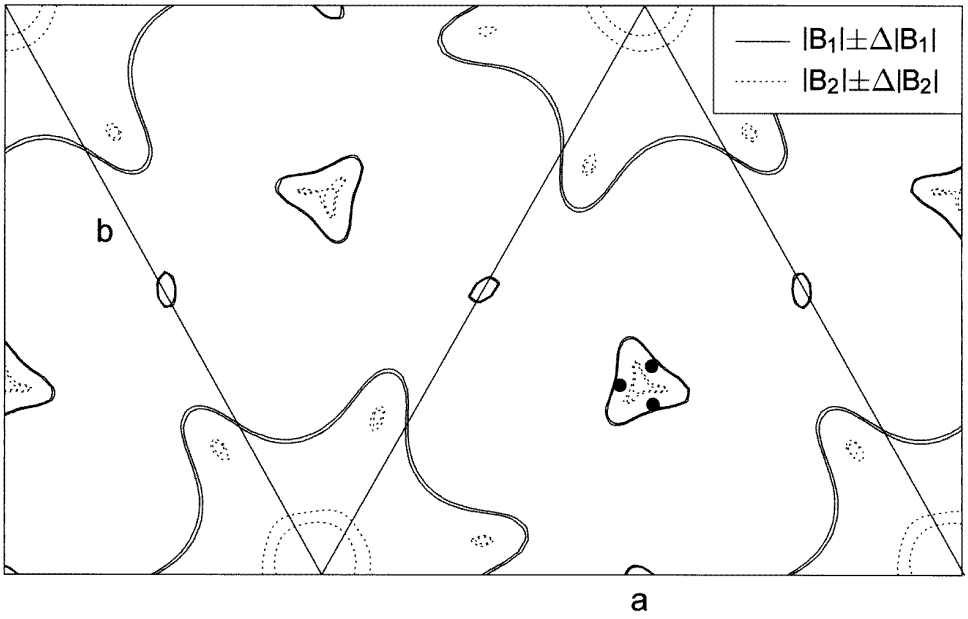

Figure 17. Calculated contour lines for the dipolar field for the ordered state in the $z = \frac{1}{2}$ plane. The lines refer to $B_1 = 2100 \pm 100$ G and $B_2 = 325 \pm 50$ G. The sites I are indicated as black dots. The site-II candidates from figure 9 fall between the B_2 contour lines.

4.2. Antiferromagnetic structure, spontaneous fields $\boldsymbol{B}_i$ and μ^+-sites

Since $U_{14}Au_{51}$ orders antiferromagnetically, $\boldsymbol{B}_i$ does not contain contributions from the demagnetization and the Lorentz fields. The only contributions are the contact hyperfine field $\boldsymbol{B}_c$ and the sum of dipolar fields $\boldsymbol{B}_{dip}$ from the ordered U 4f moments. While the dipolar fields are only determined by the antiferromagnetic structure, the contact hyperfine field is a muon-specific quantity which in the absence of the μ^+ would be quite different. There are no theories which would allow us to predict this quantity reliably for the AF state. However, we may estimate $\boldsymbol{B}_c$ from the contact coupling constant A_0, measured for the paramagnetic phase. A_0 is essentially only arising from the three nearest U1 neighbours

(e.g. atoms 1, 2 and 3 in figure 1) and is an average over their contributions, i.e.

$$A_0 = (A_0^{(1)} + A_0^{(2)} + A_0^{(3)})/3.$$

Assuming that $A_0^{(i)} \propto 1/r_i^3$, where r_i is the distance from μ^+ to the U atom i, and calculating $r_1/r_2 = 0.73$ for site I ($r_3 = r_2$), we estimate that $A_0^{(1)} = 0.44$ kG/μ_B and $A_0^{(2)} = A_0^{(3)} = 0.17$ kG/μ_B. Then

$$\boldsymbol{B}_c \simeq A_0^{(1)}\mu_1 + A_0^{(2)}\mu_2 + A_0^{(3)}\mu_3. \tag{17}$$

With $|\mu| = 2.28\ \mu_B$, it follows that $\boldsymbol{B}_c \simeq 0.6\mu_1/|\mu_1|$ kG (since the μ_1 are in the a–b plane, so is $\boldsymbol{B}_c$). $\boldsymbol{B}_{dip}$ can be calculated in the same way as the dipolar coupling constants A_{ii}^{dip}, taking the actual antiferromagnetic structure into account and using the values of the ordered moments for the U1 and U2 ions as given in reference [3]. (The lattice sum is calculated over a sphere with a radius of 50 Å $\simeq 4a$.) These calculations show that in the $z = 0$ and $z = 1/2$ planes the z-component of $\boldsymbol{B}_{dip}$ is generally zero, as expected. Figure 17 displays contour lines in the $z = 1/2$ plane for $B_{dip} = 325 \pm 50$ G and $B_{dip} = 2100 \pm 100$ G, corresponding to the measured fields B_i. As can be seen, the latter contour lines run very close to the three sites identified as the μ^+-sites I from the Knight shift analysis. Even better agreement is obtained when the estimated $\boldsymbol{B}_c$ is taken into account (see also figure 11). No other crossings are seen, and the unsymmetrical positions which are allowed according to figure 9 can now definitely be excluded. Note how closely the two lines for 2100 ± 100 G parallel each other, indicating steep gradients perpendicular to the lines. Any small lattice irregularities are thus expected to produce a relatively wide distribution of fields, explaining the rather large relaxation rates of the $B_1 = 2.10$ kG component. For completeness, we repeated the same procedure for the $z = 0$ plane. No position was found which was compatible with all of the data.

As figure 17 shows, a dipolar field of the order of 300 G is realized close to the position $(0\ 0\ \frac{1}{2})$. This is consistent with the previous conclusion that site II must be in the vicinity of position $(0\ 0\ \frac{1}{2})$. No further refinement is attempted in view of the uncertainties involved and the neglect of a possible small contact-field contribution.

Basically, the overall consistency of the present analysis confirms the complex antiferromagnetic structure and the moment values reported in reference [3]. The question is how well μSR data could distinguish between the structures suggested in reference [2] and reference [3]. Adopting the structure of reference [2] with the ordered moments aligned along the crystallographic c-axis, calculation would predict that the dipolar fields in the $z = 0$ and $z = 1/2$ planes would only show a non-zero component along this axis, in clear contradiction to the present findings. But also the field map comes out quite differently, as shown in figure 18 for the $z = 1/2$ plane, and no site consistent with the measured A_{ii}^{dip} can be identified.

4.3. Temperature dependence of the spontaneous $\boldsymbol{B}_i$

The temperature dependence of the data shown in figure 14 could be fitted perfectly by the expression

$$\nu_i(T) = \gamma_\mu B_i(T) = \nu_{0,i}\left(1 - \left(\frac{T}{T_N}\right)^{\delta}\right)^{\beta}. \tag{18}$$

The fits are represented by the solid lines in figure 14. The fitting parameters are listed in table 6 together with theoretical predictions for β [8]. As can be seen, the measured β

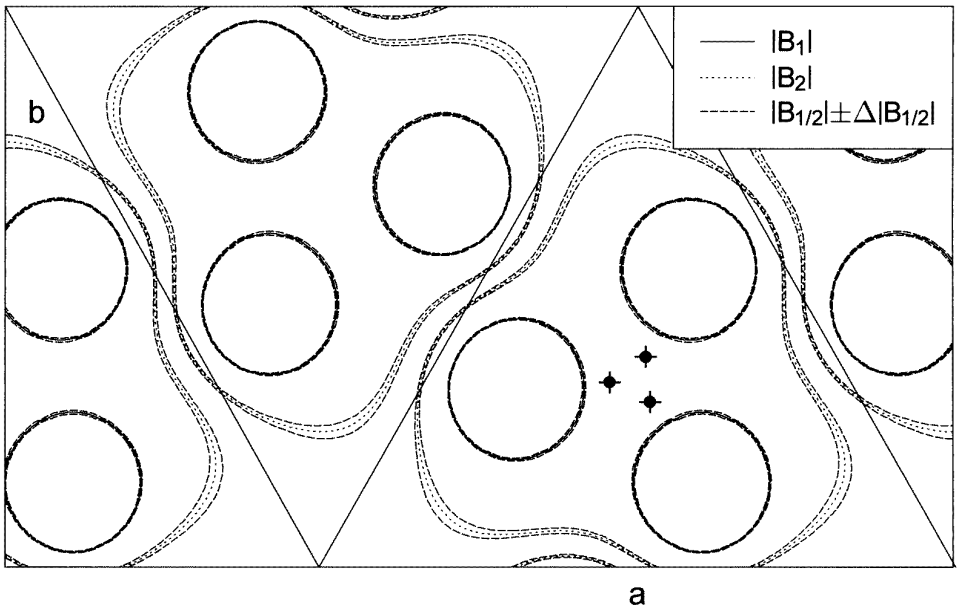

Figure 18. Calculated contour lines for the dipolar field assuming the antiferromagnetic structure proposed in reference [2]. The lines refer again to $B_1 = 2100 \pm 100$ G and $B_2 = 325 \pm 50$ G. The sites I are marked by solid circles.

are in good agreement with the predictions for a three-dimensional Heisenberg or a three-dimensional Ising magnet. The limited accuracy, however, prevents us from identifying the actual universality class. The parameter δ is introduced phenomenologically and reflects magnon excitations. In a cubic system, δ is predicted to be 2 [9]. To our knowledge, no predictions are available for a hexagonal system with different magnetic sublattices (U1, U2). The fitted parameters allow us to conclude that the temperature dependencies of the $B_i(T)$ are essentially equal. Furthermore, the $B_i(T)$ may be compared with the intensities of the magnetic Bragg peaks, $I_{ns}(T)$. One expects

$$B_i(t) \propto \sqrt{I_{ns}(T)} \propto \mu_{ord}(T).$$

We have fitted $\sqrt{I_{ns}(T)}$ also with equation (18), and the fitted parameters for the 110 reflection are listed in table 6 as well. In this case, β seems to be compatible only with a 3D Heisenberg model.

5. General discussion and conclusions

The remarkable overall consistency of the analysis of our results allowed us (i) to determine the μ^+-sites, (ii) to confirm the non-collinear antiferromagnetic structure below T_N and (iii) to conclude that the magnetic response of the U3 ions in the paramagnetic state is much reduced but not zero. The analysis produced the unexpected result that the effective Curie–Weiss temperatures θ_i' of the U1 ions next to the μ^+ are significantly different from the corresponding bulk susceptibility values (see table 1). If we had not admitted modified θ_i' in the analysis, no consistency would have been obtained. Particularly striking is the fact that also, in the basal plane, θ_i' turns out to be anisotropic. The question that immediately comes

to one's mind is of course that of how far these observations are muon induced. As regards the basal-plane anisotropy of θ_i', this may be an intrinsic feature, which is not necessarily in contradiction with the isotropy of the bulk susceptibility in the basal plane. The latter can be calculated by summing over atomic susceptibilities, whose sum by symmetry has to be isotropic in the basal plane. Indeed, just looking at one of the U1 triangles, it appears quite reasonable that it will make a difference whether the external field is applied along one of the edges of this even-sided triangle or perpendicular to it. The average susceptibility in the basal plane would be given by

$$\chi_{a,b} = \frac{1}{3}(\chi_a + 2\chi_{b^*}) = \frac{C}{3}\left(\frac{1}{T-\theta_a'} + \frac{2}{T-\theta_{b^*}'}\right) \tag{19}$$

which for $T > 0$ ($\theta_i' < 0$) can be approximated by

$$\chi_{a,b} \sim \frac{C}{T - \frac{1}{3}(\theta_a + 2\theta_{b^*}')} \tag{20}$$

and, with the values in table 1, allows us to calculate some average Curie–Weiss temperature in the basal plane: $\overline{\theta_{ab}'} \simeq -10$ K. The deviation of this average value and of θ_c' from the bulk values could still be of intrinsic origin, because the Curie–Weiss temperatures of the U2 ions in the $z = 0$ plane may also be different, and again the bulk susceptibility is an average over all U ions. If we accept this idea, we calculate for the U2 ion the following approximate Curie–Weiss temperatures: $\theta_{ab} \simeq -132$ K and $\theta_c \simeq -58$ K. These values are not unreasonable in view of the observation in reference [3] that the major part of the c-axis susceptibility below and just above T_N is due to the U2 ions. In fact, with the above effective values for θ_i', we calculate at 22 K and for an applied field of 4.6 T along the c-axis the following induced moments at the U1 and U2 ions: $\mu(\mathrm{U1}) = 0.06\ \mu_B$ and $\mu(\mathrm{U2}) = 0.15\mu_B$, which are to be compared with measured values [3] of $0.05\ \mu_B$ and $0.10\ \mu_B$, respectively. For the basal-plane susceptibility, the situation should be reversed. It would be interesting to check this conjecture by performing further polarized neutron scattering investigations.

We cannot exclude, of course, the possibility that some part of the deviation of θ_i' from the bulk values is a muon-induced effect. The μ^+ will induce some local lattice relaxation, as observed for protons in metals, changing thereby local distances, and, due to the build up of a screening cloud of conduction electrons around the μ^+, also a certain redistribution of charge has to be expected. Both effects may modify the RKKY-mediated exchange coupling among the nearest U neighbours of the μ^+, without, however, changing the Néel temperature.

The effective Curie–Weiss temperature derived from signal No 4, involving site II, is even more difficult to explain. The near-halfway position of the μ^+ between two nearest U3 neighbours implies that one monitors to a certain extent the weak magnetic response of this largely non-magnetic pair. It will be interesting to perform more precise measurements of signal No 4, which we hope to be able to do in the near future.

At present we have no idea how to interpret the other interesting parameter determined by the analysis, namely the temperature-independent contribution to the μ^+ Knight shift, K_i^0 (see table 3). In particular, its anisotropy is a very unusual property. Its values are reasonable and of the same order of magnitude as for other intermetallic systems. Most probably it arises from the Pauli paramagnetism of the conduction electrons screening the μ^+-charge, but the appearance of a negative sign indicates that p-type and/or d-type electrons are possibly also involved, as is known from other metallic systems consisting of, or containing, transition and/or 4f and 5f elements [10].

Another puzzling observation concerns the behaviour of the relaxation rates λ_1 and λ_2 for the ordered state. While the low-temperature ratio $\lambda_1/\lambda_2 \approx \omega_1/\omega_2$ suggests that the λ_i reflect the width ΔB_i of the static-field distribution around each average field B_i, scaling with B_i ($\Delta B_i/B_i = \lambda_i/\gamma_\mu B_i \simeq 0.28$ at low T is not untypical for intermetallic compounds and reflects the crystal quality and perfection of the ordered magnetic structure), the slight increase of λ_2 and the essentially linear decrease of λ_1 with rising temperature up to 19 K (at and above 19 K, $\lambda_1 \simeq \lambda_2$) is unexpected and seemingly contradictory. It raises the suspicion that the μ^+ at site II are somehow affected by the two nearest-neighbour U3 ions. Perhaps the U3-ion pair is the source of strong fluctuating fields which induce μ^+ spin–lattice relaxation at site II. On the other hand, above T_N, signal No 4 shows the slowest relaxation. Whether a dynamic origin of λ_2 is indeed indicated will have to be studied by longitudinal-field-decoupling experiments.

Yet another unusual result concerns the occupation probabilities of the two sites I and II as reflected in the respective signal amplitudes. These probabilities are related to the depth of the potential 'felt' by the μ^+ at the respective sites. The depth will depend on the local geometry and distances. According to figure 17, far below T_N more μ^+ are found at site I than at site II. With rising temperature, the population of site II grows at the expense of that of site I and dominates near T_N. In contrast, figure 6 shows that the population of site II decreases above T_N and site I becomes the dominantly occupied site up to about 210 K, before the onset of diffusion obscures the picture. It thus seems that the occupation probabilities are affected by the magnetic phase transition and the occupation of site II approaches a maximum near or at T_N. Since the lattice parameters and also the atomic positions depend only very little on temperature [2], they cannot be responsible for the observed temperature dependence. Usually the self-trapped state of the μ^+ is viewed as a small polaron. The energy gained by the small lattice expansion induced around the μ^+ depends on certain elastic stiffness constants C_{ij} [11]. Therefore, we conjecture that the occupation probabilities could depend on the temperature dependence of the elastic stiffness tensor. Unfortunately, nothing is known about the elastic properties of $U_{14}Au_{51}$.

In summary, the present study has demonstrated that μSR spectroscopy has the potential to also investigate complicated antiferromagnetic structures, provided that the μ^+-site can be determined as well. In particular, different magnetic structures (such as the ones proposed in references [2] and [3]) can clearly be distinguished by the μSR technique. We stress that, whenever possible, a magnetic structure determination should only be relied upon if neutron scattering and μSR investigations yield consistent results. There are several examples for which the magnetic structure deduced from neutron scattering data is severely at odds with μSR results (e.g. CeB_6 [12, 13], CeTSn (T = Pd, Pt) [14, 15] and $HoBa_2Cu_3O_7$ [16, 17]). In view of the present experience, it is suggested that one should reconsider the analysis of the neutron data for the above-mentioned and other compounds. A new feature, not envisioned before, is the observation that, for the paramagnetic state, the individual magnetic responses of magnetic ions at crystallographically inequivalent sites can be distinguished and more or less be determined quantitatively. An obstacle to a straightforward determination is the possibility that the presence of the μ^+ may induce modifications in the local susceptibility. Such modifications are known to exist and can quantitatively be accounted for in the case in which the low-temperature behaviour of the magnetic susceptibility is governed by the crystalline-electric-field splitting of the electronic ground state [5]. The possibility, as discussed above, that local Curie–Weiss temperatures may also be modified has not been demonstrated beyond doubt so far. Progress may be achieved by studying systems in which only one type of magnetic ion at a unique crystallographic site is present and where CEF effects can be ignored.

References

[1] Ott H R, Felder E, Schilling A, Dommann A and Hulliger F 1989 *Solid State Commun.* **71** 549
[2] Dommann A, Ott H R, Hulliger F and Fischer P 1990 *J. Less-Common Met.* **160** 171
[3] Brown P J, Crangle J, Neumann K-U, Smith J G and Ziebeck K R A 1997 *J. Phys.: Condens. Matter* **9** 4729
[4] Schenck A 1985 *Muon Spin Rotation Spectroscopy—Principles and Applications in Solid State Physics* (Bristol: Hilger)
Brewer J H 1994 *Encyclopedia of Applied Physics* vol 11, ed G L Trigg (New York: VCH) p 23
[5] Feyerherm R, Amato A, Grayevsky A, Gygax F N, Kaplan N and Schenck A 1995 *Z. Phys.* B **99** 3
[6] Schenck A and Gygax F N 1995 *Handbook of Magnetic Materials* vol 9, ed K H J Buschow (Amsterdam: Elsevier) p 60
[7] Akishin P G and Gaganov I A 1992 *J. Magn. Magn. Mater.* **110** 175
[8] Binney J J, Dowrich N J, Fisher A J and Newman M E J 1992 *The Theory of Critical Phenomena* (Oxford: Oxford University Press)
[9] Kubo R 1952 *Phys. Rev.* **87** 568
[10] Examples include UPd_2Al_3 and U_2Zn_{17} with $K_0 \simeq -(200–250)$ ppm (unpublished results).
[11] Kehr K W 1978 *Hydrogen in Metals I* ed G Alefeld and J Völkl (Berlin: Springer)
[12] Effantin J M, Rossat-Mignod J, Burlet P, Bartholin H, Kunii S and Kasuya T 1985 *J. Magn. Magn. Mater.* **47+48** 145
[13] Feyerherm R, Amato A, Gygax F N, Schenck A, Ōnuki Y and Sato N 1995 *J. Magn. Magn. Mater.* **140+144** 1175
[14] Kadowaki H, Ekino T, Iwasaki H, Takabatake T, Fujii H and Sakura J 1993 *J. Phys. Soc. Japan* **62** 4426
[15] Kalvius G M, Kratzer A, Münch K-H, Takabatake T, Nakamoto G, Fujii H, Wäppling R, Klauss H-H, Kiefl R, Kreitzmann S and Noakes D R 1994 *Hyperfine Interact.* **85** 411
[16] Roessli B, Fischer P, Staub U, Zolliker M and Furrer A 1993 *Europhys. Lett.* **23** 511
[17] Birrer P, Gygax F N, Hitti B, Lippelt E, Schenck A, Weber M, Barth S, Hulliger F and Ott H R 1989 *Phys. Rev.* B **39** 11 449
Pinkpank M 1997 unpublished results (PSI)